Pore scale mixing and macroscopic solute dispersion regimes in polymer flows inside two-dimensional model networks

Maria Veronica D'Angelo[a)]
Laboratoire Fluides, Automatique et Systèmes Thermiques, UMR 7608, Universités Pierre et Marie Curie, Paris 6 et Paris-Sud, Bâtiment 502, Campus Paris Sud, 91405 Orsay Cedex, France
and Grupo de Medios Porosos, Facultad de Ingenieria, Paseo Colon 850, 1063 Buenos Aires, Argentina

Harold Auradou,[b)] Catherine Allain, and Jean-Pierre Hulin[c)]
Laboratoire Fluides, Automatique et Systèmes Thermiques, UMR 7608, Universités Pierre et Marie Curie, Paris 6 et Paris-Sud, Bâtiment 502, Campus Paris Sud, 91405 Orsay Cedex, France

(Received 2 November 2006; accepted 9 February 2007; published online 28 March 2007)

A change of solute dispersion regime with the flow velocity has been studied both at the macroscopic and pore scales in a transparent array of capillary channels, using an optical technique allowing for simultaneous local and global concentration mappings. Two solutions of different polymer concentrations (500 and 1000 ppm) have been used at different Péclet numbers. At the macroscopic scale, the displacement front displays a diffusive spreading: for $\mathrm{Pe} \leq 10$, the dispersivity l_d is constant with Pe and increases with the polymer concentration; for $\mathrm{Pe} > 10$, l_d increases as $\mathrm{Pe}^{1.35}$ and is similar for the two concentrations. At the local scale, a time lag between the saturations of channels parallel and perpendicular to the mean flow has been observed and studied as a function of the flow rate. These local measurements suggest that the change of dispersion regime is related to variations of the degree of mixing at the junctions. For $\mathrm{Pe} \leq 10$, complete mixing leads to pure geometrical dispersion enhanced for shear thinning fluids; for $\mathrm{Pe} > 10$, weaker mixing results in higher correlation lengths along flow paths parallel to the mean flow and in a combination of geometrical and Taylor dispersion. © *2007 American Institute of Physics*. [DOI: 10.1063/1.2714065]

I. INTRODUCTION

The problem of solute transport in porous media is relevant to many environmental, water supply, and industrial processes.[1,2] In addition, tracer dispersion is a useful tool to analyze porous media heterogeneities.[3] Solute dispersion is often measured by monitoring solute concentration variations at the outlet of the sample following a pulse or step-like injection at the inlet: Understanding fully the dispersion mechanisms, however, requires information on the local concentration distribution and on local mixing at the pore scale. These goals can be reached by using nuclear magnetic resonance imaging, computerized axial tomography (CAT) scan, or acoustical techniques.[4] However, such techniques are either costly or have a limited resolution. In addition, they often put strong constraints on the characteristics of the fluid pairs. We used instead in the present work a two-dimensional (2D) transparent square network of ducts of random widths allowing for easy visualizations of mixing and transport processes at the local scale. Similar systems were previously used successfully to investigate two phase flows[5] and miscible displacements of Newtonian fluids.[6]

The key feature of the present experiments is to combine macroscopic and local scale measurements to estimate the influence of pore scale processes on dispersion. For this purpose, dye is used as a solute and high-resolution maps of the relative concentration distribution are obtained through calibrated light absorption measurements. This allows one to determine quantitatively the global dispersion coefficient D and the dispersivity l_d while measuring simultaneously the time lag between the invasion of channels parallel and transverse to the mean flow. Further information is also obtained from the complex geometry of an isoconcentration line.

This approach has allowed us to observe a change of macroscopic dispersion regime for a Péclet number of the order of 10 while the local measurements suggest interpretations in terms of variations of the degree of mixing at the junctions. This confirms previous suggestions[7,8] on the influence of mixing at the pore scale on macroscopic dispersion.

Another feature of our experiments is the use of shear thinning polymer solutions of the type encountered in many industrial processes in petroleum, chemical, and civil engineering.[9] In addition to these practical applications, previous measurements at the laboratory scale on glass bead packings have shown[10,11] a significant enhancement of tracer dispersion compared to the Newtonian case. This enhancement depends on the polymer concentration and represents a useful additional input for our interpretations.

II. DISPERSION MECHANISMS IN 3D POROUS MEDIA AND 2D NETWORKS

In homogeneous 3D porous media, the macroscopic concentration $\bar{C}(x,y,z,t)$ of a tracer (i.e., averaged over a repre-

[a)]Electronic mail: vdangelo@fi.uba.ar
[b)]Electronic mail: auradou@fast.u-psud.fr
[c)]Electronic mail: hulin@fast.u-psud.fr

sentative elementary volume) satisfies the convection-diffusion equation,

$$\frac{\partial \bar{C}}{\partial t} = U\frac{\partial \bar{C}}{\partial x} + D_{\parallel}\frac{\partial^2 \bar{C}}{\partial x^2} + D_{\perp}\left[\frac{\partial^2 \bar{C}}{\partial y^2} + \frac{\partial^2 \bar{C}}{\partial z^2}\right], \quad (1)$$

where U the mean velocity of the fluid (parallel to x) and $D_{\parallel}$ ($D_{\perp}$) is the longitudinal (transverse) dispersion coefficient. When the concentration distribution is uniform in the directions perpendicular to the mean flow, the $D_{\perp}$ term cancels out and only $D_{\parallel}$ needs to be taken account leading to a 1D equation. This assumption may be assumed to be valid for the transparent model and for the injection method used in the present work, and the 1D version of Eq. (1) will be satisfied by the concentration distribution [practically, $\bar{C}(x,t)$ will be taken equal to an average of the local concentration over an interval Δy in the direction perpendicular to the flow]. The simpler notation D will then be used for the corresponding longitudinal dispersion coefficient.

The value of D is determined by two main physical mechanisms: molecular diffusion and advection by the complex velocity field inside the medium (the local flow velocity varies both inside individual flow channels and from one channel to another). The relative order of magnitude of these two effects is characterized by the Péclet number: $\mathrm{Pe} = Ua/2D_m$ (D_m is the molecular diffusion coefficient and a a characteristic length of the medium, here the average channel width).

Various dispersion regimes are observed in usual porous media.[1] At very low Péclet numbers ($\mathrm{Pe} < 1$), molecular diffusion is dominant and smooths out local concentration variations.

At higher Pe values, the distribution of the channel widths induces short-range variations of the magnitude and the direction of the local velocity. One can then consider that tracer particles experience a random walk inside the pore volume with a velocity varying both in magnitude and direction relative to the mean flow velocity **U**. The typical length l of the channels represents the length of the steps, and their characteristic duration τ is $\tau \approx l/U$. A classical feature of random walks is that the corresponding diffusion coefficient satisfies $D \propto l^2/\tau = Ul$. The proportionality constant depends both on the disorder of the medium and on the rheology of the fluid. In this so-called *geometrical dispersion*, the coefficient D should then be proportional to U.

The 2D networks of interest in the present work have several specific features and D should be very much influenced by the redistribution of the incoming tracer between the channels leaving a junction. This redistribution strongly depends on the local structure of the flow field and on the Péclet number.[12,13] At low Pe values, the transit time through a junction is large enough for tracer to cross streamlines by molecular diffusion and one may assume a perfect mixing. In the other limit $\mathrm{Pe} \gg 1$, molecular diffusion is negligible: the path of the tracer particles coincides with the flow lines and is determined by the flow field in the junctions and by the location of the particles in the flow section.

In the case of 2D networks with small variations of the channel apertures, the flow field is close to that in a periodic square channel with a mean flow parallel to one of the axis: the major part of the flow is localized in longitudinal channels parallel to the axis where the velocity is high, while that in transverse channels is small. Tracer particles remain then inside sequences of channels parallel to the mean flow for a long distance without moving sideways. Taylor-like dispersion[14,15] similar to that encountered in capillary tubes, between parallel plates or inside periodic structures, may then develop: it corresponds to a balance between (a) spreading due to velocity gradients between the centers of the flow channels and their walls and (b) molecular diffusion across the flow lines. The increased dispersion in 2D periodic networks when flow is parallel to one of the axes[7] may, for instance, result from the increased influence of Taylor dispersion.

Another issue of the present work is the influence of the shear-thinning properties of the fluids. They may influence the dispersion process in different ways: on the one hand, when the viscosity μ decreases with the shear rate $\dot{\gamma}$, the velocity profile in individual channels becomes flat in the center of the channel. In simple geometries like capillary tubes, the corresponding Taylor dispersion coefficient D is then lower than for a Newtonian fluid, although one has still $D \propto \mathrm{Pe}^2$.[16] On the other hand, numerical investigations suggest that the flow of shear thinning fluids is localized in a smaller number of flow paths than for Newtonian fluids.[17,18] As a result, geometrical dispersion reflecting the distribution of the local velocities should increase, as is indeed observed experimentally.[10,11] A key point here is the influence of the fluid rheology on tracer mixing at the intersections between channels: to our knowledge, no previous experimental or numerical work has dealt with this crucial issue.

III. EXPERIMENTAL SETUP AND PROCEDURE

A. Experimental models and injection setup

The model porous medium is a two-dimensional square network of channels of random aperture: these models have been realized by casting a transparent resin on a photographically etched mold as described in Ref. 5. The model contains a square network of 140×140 channels with an individual length equal to $l = 0.67$ mm and a depth of 0.5 mm; the width follows a discrete, log-normal distribution with seven values between 0.1 and 0.6 mm [the average width is $\bar{a} = 0.33$ and its standard deviation $\sigma(a) = 0.11$ mm]. The mesh size of the network is equal to 1 mm. The overall size of the model is 150×140 mm and the two facing lateral sides are sealed. On the two others, the channels are directly connected to the outside. The total pore volume is close to 6.09×10^3 mm^3. Following the definition of Bruderer *et al.*,[19] the degree of heterogeneity of the network can be characterized by the normalized standard deviation $\sigma(a)/\bar{a}$. In the present work, $\sigma(a)/\bar{a} \simeq 0.33$.

B. Fluid preparation and characterization

The fluids used in the experiments are shear thinning water-polymer solutions. The shear thinning fluids are solutions of 500–1000 ppm of high molecular weight scleroglu-

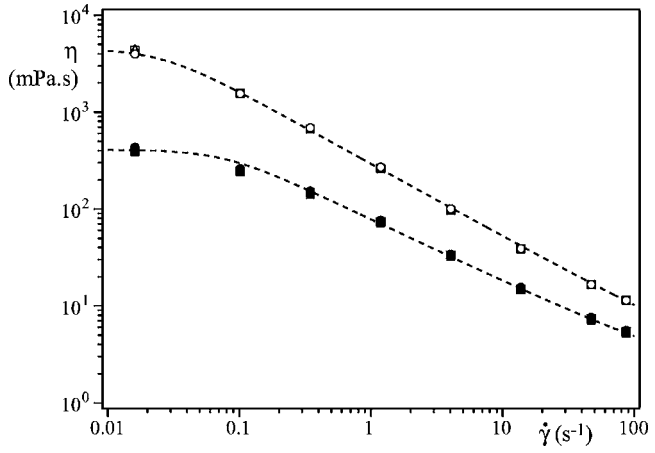

FIG. 1. Variation of the effective viscosity η of the polymer solutions as a function of the shear rate $\dot{\gamma}$ for two water-polymer solutions of different concentrations. 500 ppm: (▲) clear solution; (■) same with 200 ppm dye; (●) dyed solution after two weeks. 1000 ppm: (△) fresh clear solution; (□) same after four days; (○) same after six weeks. The dotted lines represent Carreau functions corresponding to the sets of parameters of Table I.

can in high-purity water (Millipore—Milli-Q grade). Scleroglucan (Sanofi Bioindustries, France) is a polysaccharide with a semirigid molecule (persistence length $\simeq 180 \times 10^{-9}$ m); it has been selected because it is electrically neutral and its characteristics are therefore independent of the ion (and dye) concentration. All solutions are protected from bacterial contamination by adding 0.2 g/l of NaN_3. In all experiments, the injected and displaced fluids are identical except for Water Blue dye, which is added to one of the solutions at a concentration of 200 ppm by weight to allow for optical concentration measurements.

The molecular diffusion coefficient of the dye is determined independently in pure water by means of Taylor dispersion measurements performed separately in a capillary tube (the measured value of D_m was close to 6.5×10^{-4} mm^2 s^{-1}).

The rheological properties of the scleroglucan solutions have been characterized using a *Contraves LS30* Couette rheometer with shear rates $\dot{\gamma}$ ranging from 0.016 up to 87 s^{-1}. Rheological curves obtained experimentally for the two polymer concentrations are displayed in Fig. 1: these curves display the variation of the effective viscosity η (ratio of the stress and the shear rate $\dot{\gamma}$ for a given value of $\dot{\gamma}$) as a function of $\dot{\gamma}$. The properties of 500 ppm clear and dyed solutions are identical within experimental error and constant with time over a period of two weeks. The properties of two 1000 ppm solutions realized independently are reproducible and constant over a period of six weeks (for the second solution).

The variation of η with $\dot{\gamma}$ is well adjusted by a Carreau function (dotted lines in Fig. 1),

$$\eta = \frac{1}{\left[1 + \left(\frac{\dot{\gamma}}{\dot{\gamma}_0}\right)^2\right]^{(1-n)/2}}(\eta_0 - \eta_\infty) + \eta_\infty. \quad (2)$$

The values of these different rheological parameters for the polymer solutions used in the present work are listed in Table I; determining η_∞ would have required values of $\dot{\gamma}$ outside the measurement range so that we assume that $\eta_\infty = 10^{-3}$ Pa s (the value for the solvent, i.e., water). In Eq. (2), $\dot{\gamma}_0$ corresponds to a crossover between two regimes. On the one hand, for $\dot{\gamma} < \dot{\gamma}_0$, the viscosity η tends toward η_0, and the fluid displays a Newtonian behavior ("Newtonian plateau" regime). On the other hand, for $\dot{\gamma} \gg \dot{\gamma}_0$, the effective viscosity decreases with the shear rate following the power law $\eta \propto \dot{\gamma}^{(n-1)}$ ($n=1$ for a Newtonian fluid.) It should finally be noted that the high effective viscosity of these solutions at low shear rates avoids the appearance of buoyancy-induced instabilities at low shear rates and helps stabilize the fluid displacement.

TABLE I. Rheological parameters of scleroglucan solutions used in the flow experiments.

Polymer conc. ppm	n	$\dot{\gamma}_0$ s^{-1}	η_0 mPa s
500	0.38±0.04	0.077±0.018	410±33
1000	0.26±0.02	0.026±0.004	4500±340

Such a stabilizing effect might also be obtained by using high-viscosity Newtonian fluids, but this would result in potentially destructive overpressures at high flow velocities. More importantly, the molecular diffusion coefficient would decrease as the inverse of the viscosity, which would disturb strongly the mixing process; on the contrary, for the polymer solutions, the molecular diffusion coefficient is almost identical to that of the solvent and is practically independent of the effective viscosity of the fluid.

C. Fluid injection and flow visualization

The model is placed vertically with its open sides horizontal: the upper side is fitted with a leak tight adapter allowing one to suck fluid upwards. The lower open side is initially slightly dipped into a bath of one of the liquids and is saturated with this fluid by pumping it slowly upwards. After switching off the pump, the bath can be lowered until it no longer touches the model (Fig. 2). The bath is then completely emptied, refilled with the other fluid, and raised to its initial position. Finally, the first fluid is sucked upwards at the upper end of the model by the syringe pump. The lower bath rests upon computer controlled electronic scales for monitoring the amount of fluid that has entered the model.

This procedure allows one to obtain a front of the displacing fluid that is initially perfectly straight: this uniform injection of dye across the full width of the model (in the y direction) insures that front spreading reflects only longitudinal dispersion as long as the medium does not display any large permeability heterogeneity.

The flow rates used in the experiments correspond to mean front velocities between 0.005 and 2.5 mm s^{-1}. Assuming a channel width of 0.4 mm, the corresponding typical shear-rate is of the order of 0.025 s^{-1}: this is lower than the value $\dot{\gamma}_0$ marking the transition toward the "Newtonian plateau regime" for the 500 ppm solution but comparable for

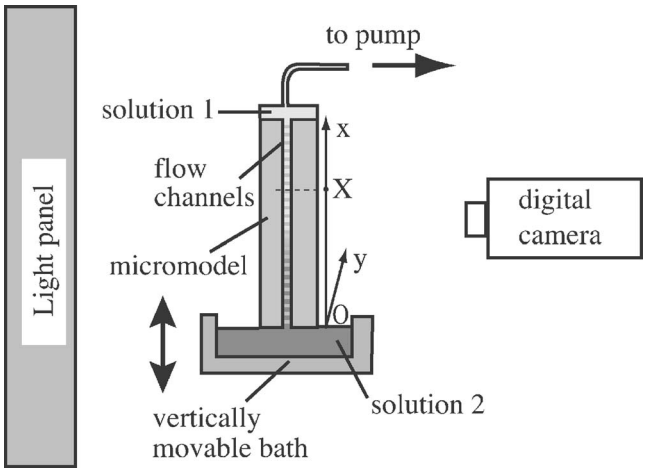

FIG. 2. Experimental setup for miscible displacement measurements in 2D micromodels. Flow is vertical and parallel to the x axis. The width of the channel network is horizontal and parallel to the y axis.

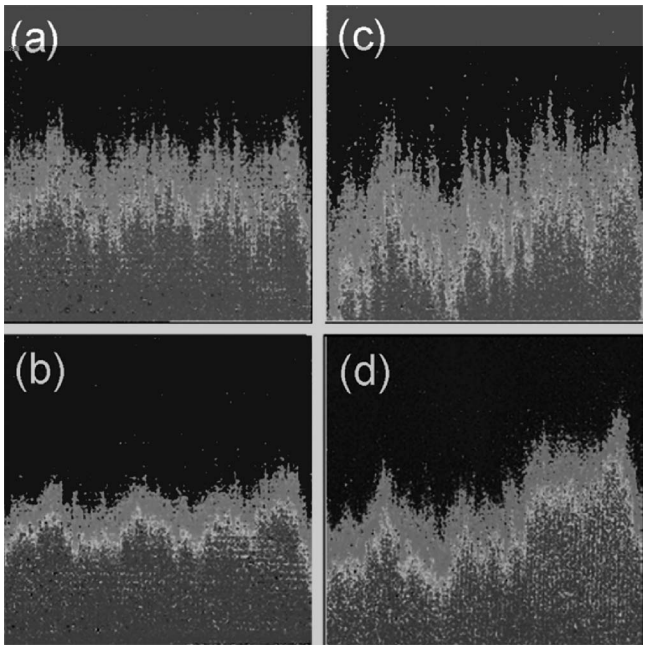

FIG. 3. Relative concentration maps for experiments using water-scleroglucan solutions of respective concentrations 500 ppm [(a) and (b)] and 1000 ppm [(c) and (d)] for flow rate values $Q=0.075$ ml/mn [(b) and (d)] and $Q=1.5$ ml/mn [(a) and (c)]. Gray levels code used in the figure: darkest shade=pure displaced fluid, intermediate–pure displacing fluid–lightest=intermediate concentrations.

the 1000 ppm one (see Table I). At the lowest velocities attainable, the 500 ppm solution should therefore give similar results as a Newtonian fluid of high viscosity η_0 but with the same molecular diffusion coefficient as for water while the 1000 ppm one will retain its shear thinning character.

The model is illuminated from the back by an electronic light panel and images are acquired by a 12-bit, high stability digital camera with a 1030×1300 pixels resolution and then recorded by a computer. The pixel size is 0.16 mm or 0.4 times the mean width of the channels: this allows one to discriminate between the various regions of the pore space. Typically 100 images are recorded for each experimental run at time intervals from 2.5 to 700 s.

D. Image analysis procedure

The images are then translated into maps of the relative concentration using the following procedure. First, a calibration curve is obtained from images of the model saturated with seven solutions of increasing dye concentration C starting from zero up to the concentration used in the experiments. The logarithm $\mathrm{Ln}[I(C)/I_o]$ of the transmissivity is then plotted as a function of C; $I(C)$ and I_o are averages of the light intensity over the model and correspond, respectively, to dye concentrations equal to C and 0. Due to the nonlinear absorbance effect,[20] a better fit is obtained with a third-order polynomial variation of $\mathrm{Ln}[I(C)/I_o]$ with C than with the linear dependence corresponding to Lambert's law. This calibration is performed every time the locations of the light source and of the models are significantly changed.

For all experiments, reference images are recorded both with the micromodel initially saturated with the displaced fluid and, at long times, when it is fully saturated with the injected one. After the fluid displacement has been performed, the local concentrations are determined pixel by pixel for each image by means of the calibration curve. This operation is performed only on pixels belonging to channels; those located in solid parts are not considered. Finally, maps of the local *relative* concentration of the two fluids are obtained by normalizing the local concentration between its values in the initial and final images.

IV. EXPERIMENTAL RESULTS

A. Qualitative observations of miscible displacements

Figure 3 compares displacement experiments realized at the same flow velocity for the two water-scleroglucan solutions. For a given solution, narrow structures of the front with a lateral extent of a few channel widths appear when the velocity increases and reflect local high- or low-velocity zones. For the same flow rate, images obtained with the two solutions are qualitatively similar: the size parallel to the flow of medium scale front structures (with a width Δy of the order of one-tenth of that of the model) is, however, larger for the more concentrated solution both at low and high velocities.

The stability of the displacement with respect to buoyancy driven instabilities has also been verified by comparing experiments using the same pair of fluids and exchanging the injected and the displaced fluid: no quantitative difference was measured between the two configurations and no fingering instabilities appeared in the unstable configuration.

While fluid displacement images provide information on the front geometry down to a fraction of the channel size, it will be shown next that they also allow one to determine macroscopic parameters characterizing the process.

B. Quantitative dispersion measurement procedure

Quantitatively, the global displacement process is analyzed from the variations with time and distance parallel to

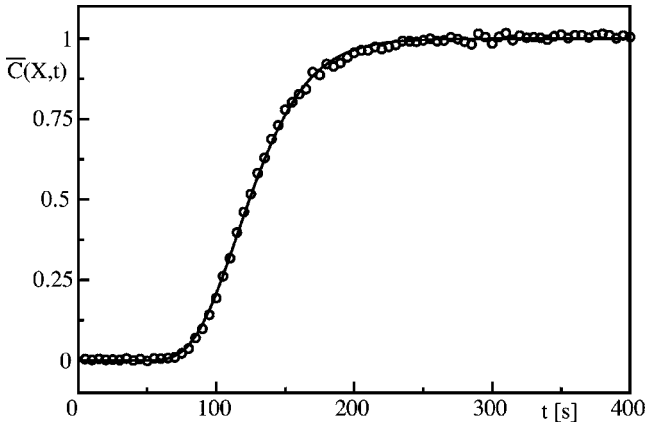

FIG. 4. Normalized concentration variation $\bar{C}(x,t)$ as a function of time for a displacement experiment using a 500 ppm polymer solution with $Q=3.75$ ml/mn. $\bar{C}(x,t)$ is computed by averaging local concentration over an interval $\Delta y \simeq 35$ mm located in the central part of the model. Distance from inlet: $X=100$ mm. Continuous line: fit by Eq. (3).

the flow of a macroscopic concentration $\bar{C}(X,t) = \langle \bar{C}(X,Y,t) \rangle_Y$; the average is taken over an interval ΔY perpendicular to the flow and only pixels located inside the pore volume are considered. The width ΔY is large enough to average out local fluctuations and small enough to avoid the influence of the side walls: $\bar{C}$ was found to be independent of Δy within experimental error when these conditions are verified. Even when Δy corresponds to only one channel, it will be seen below that the results are all but similar. Figure 4 displays a typical variation of $\bar{C}(X,t)$ with time. For step-like initial concentration variations corresponding to our experiments, the solution of the convection-dispersion equation (1) is

$$\bar{C} = \frac{1}{2}\left[1 - \mathrm{erf}\frac{t-\bar{t}}{\sqrt{4\frac{D}{U^2}t}}\right]. \tag{3}$$

As seen in Fig. 4, a very good fit of the experimental data with this solution (continuous line) is obtained by adjusting the two parameters of the equation, namely the mean transit time $\bar{t}$ and the ratio $D/U^2 (= \bar{\Delta}t^2/2\bar{t}$, where $\bar{\Delta}t^2$ is the centered second moment).

Figure 5 displays the variation of the mean transit time $\bar{t}$ with the distance X from the inlet for two very different flow rates: $\bar{t}$ increases in both cases linearly with distance, indicating that the mean velocity U is constant and can be determined by a linear regression of the data. The inset (magnified view of the curve) shows that, in both cases, $\bar{t}(X)$ oscillates about the mean trend (dotted line) corresponding to the linear regression. The dependence of the amplitude of these oscillations on Pe and on the rheology of the fluid will be investigated systematically in Sec. IV D.

Similar features are observed on the variation of the dispersion coefficient D plotted in Fig. 6 as a function of the distance X from the injection (D is computed from the value of D/U^2 given by the fit with U equal to $X/\bar{t}$). This time, $D(X)$ is globally constant with X; like $\bar{t}$, it displays periodic

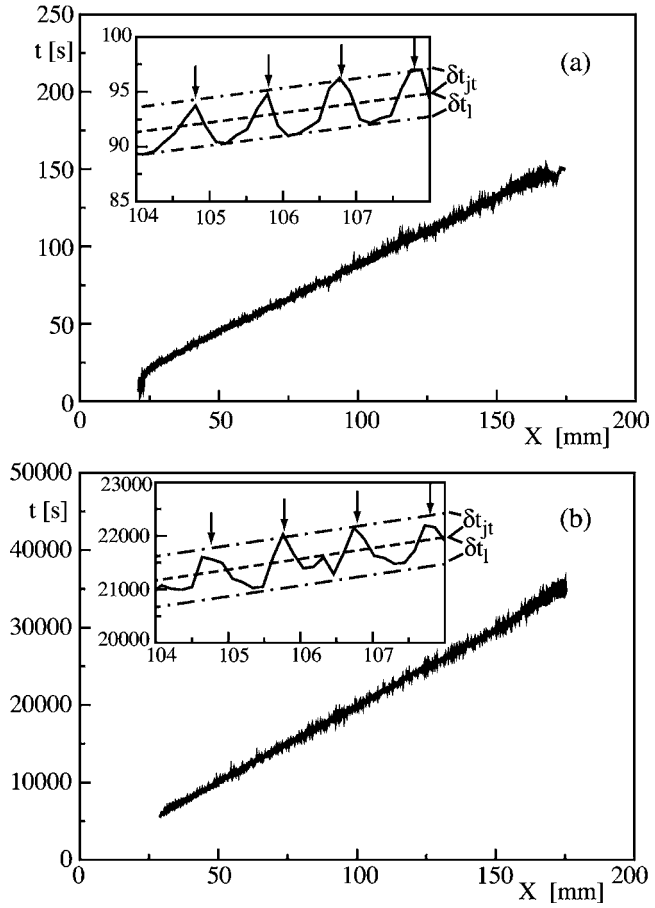

FIG. 5. Variation of $\bar{t}$ with the distance X (polymer concentration: 500 ppm), for dyed fluid displacing clear fluid. Inset: close-up view including four channels. Vertical arrows: location of junctions between channels. Dashed line: linear regression of the variation of $\bar{t}$ with X. Dash-dotted lines: mean trend of maximum and minimum values of $\bar{t}$ for different distances from the inlet (δt_{jt} and δt_l=mean amplitudes of the upwards and downwards deviations from the linear regression). (a) Mean velocity $U=1.25$ mm/s, Pe $=320$, $\delta t_{jt}=2.1$ s, $\delta t_l=-2.1$ s; (b) $U=0.05$ mm/s, Pe$=1.3$, $\delta t_{jt}=450$ s, $\delta t_l=-450$ s.

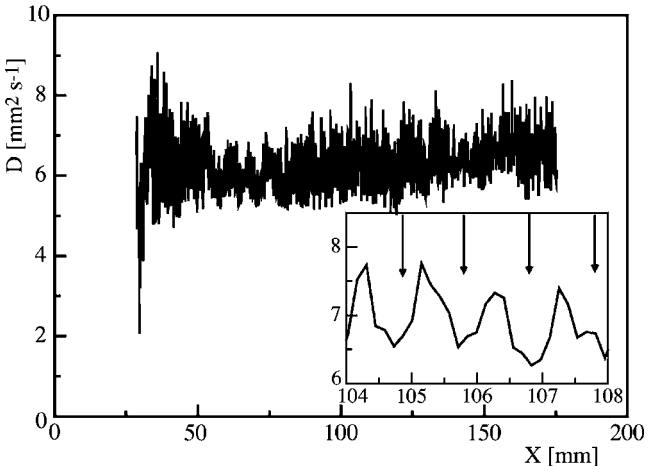

FIG. 6. Variation of D with the distance X for dyed fluid displacing clear fluid (polymer concentration: 500 ppm, $Q=3.75$ ml/min, Pe$=317$). Inset: close-up view including four channels. Vertical arrows: junctions between flow channels.

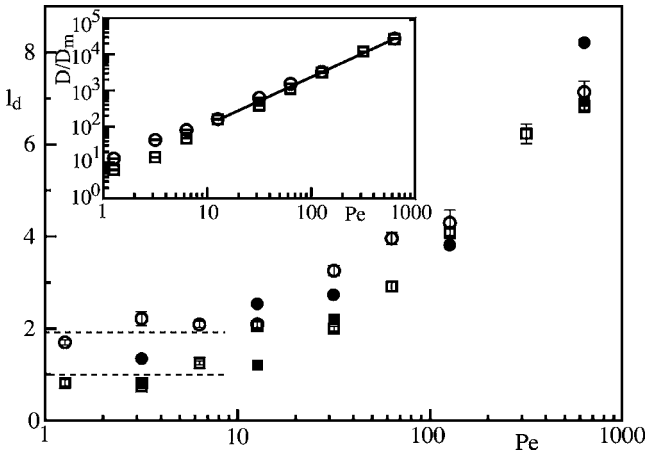

FIG. 7. Variation of the dispersivity l_d (mm) with the Péclet number for experiments with water-polymer solutions: (□), (■): 500 ppm concentration; (○), (●): 1000 ppm. Open (dark) symbols: averaging interval: 35 (0.4) mesh sizes. Inset: variation of normalized dispersion coefficient D/D_m as a function of the Péclet number for two polymer concentration (same symbols as in the main graph). Solid line: power law fit for $\mathrm{Pe}>10$ (exponent 1.33 ± 0.03). Dotted lines: average of the values of l_d corresponding to $\mathrm{Pe}<10$.

oscillations related to the structure of the network, which will be discussed below. While these curves have been obtained for dyed fluid displacing clear fluid, comparison experiments have been realized with clear fluid displacing dyed fluid; no systematic difference between the two sets of data was observed, confirming that there are no buoyancy driven instabilities.

The oscillations of $\bar{t}$ and D as X varies are closely related to mixing at the junctions and to the exchange of tracers between the transverse channels and the rest of the flow (a quantitative analysis will be presented in Sec. IV D).

The above analysis has been performed for all experiments realized with both polymer concentrations. In the following section, variations with Pe of the dispersion coefficient D measured in this way are discussed.

C. Flow velocity dependence of dispersion coefficient

The variations with the Péclet number Pe of the dispersion coefficient D determined as explained in the previous section are displayed in the inset of Fig. 7. For both polymer concentrations, D always increases with Pe but two different variation regimes are visible.

For $\mathrm{Pe}\geq10$, values of D corresponding to the two polymer concentrations fall on top of each other and increase like $D\sim\mathrm{Pe}^{\beta}$ with $\beta=1.33\pm0.03$. This is in good agreement with numerical simulations[19] realized for a similar geometry and degree of heterogeneity [as characterized by $\sigma(a)/\bar{a}=0.33$] and for which a power-law variation with an exponent of the order of 1.3 is also obtained. The difference between this exponent and the value $\beta=1$ corresponding to geometrical dispersion is therefore higher than the experimental error even if a logarithmic correction factor such that $D\propto\mathrm{Pe}\ \mathrm{Log}\ \mathrm{Pe}$ is introduced.[21] A likely hypothesis is that this variation reflects a crossover from geometrical dispersion ($D\propto\mathrm{Pe}$) to Taylor dispersion ($D\propto\mathrm{Pe}^2$): in that range of Péclet numbers, both mechanisms would then contribute to the dispersion process.

For $\mathrm{Pe}<10$, on the contrary, values of D obtained for the 1000 ppm polymer solution are higher than those obtained with the 500 ppm one. The variation of D with Pe in that range has been studied more precisely by plotting the dispersivity $l_d=D/U$ in the main graph of Fig. 7. The value of l_d is approximately constant for $\mathrm{Pe}<10$ for both polymer concentrations and its mean is significantly larger for the 1000 ppm solution ($l_d=1.95\pm0.25$ mm) than for the 500 ppm one ($l_d=1\pm0.25$ mm). This implies that, in this range of Péclet numbers, the geometrical mechanism controls dispersion and that the corresponding dispersivity increases with the polymer concentration (at higher Pe values, l_d is, in contrast, almost identical for the two solutions).

The values plotted in Fig. 7 have been obtained by averaging the concentration C over 35 channels in the direction perpendicular to the mean flow. In order to estimate the influence of the heterogeneities of the network, we performed an analysis in which the concentration C is only averaged over $\Delta y=4$ pixels (or about 0.55 mesh sizes of the lattice): the coordinates y of these measurement lines are chosen so that all pixels are inside a single row of successive longitudinal channels connecting the inlet and the outlet of the micromodel. The dispersivity in these channels is determined as above.

These values of l_d are represented as dark symbols in Fig. 7 and are only slightly lower than those obtained for $\Delta y=35$ mm. This result confirms that the macroscopic longitudinal dispersivity l_d is independent of the averaging width (no large-scale heterogeneity must, however, be present in the averaging domain, as is indeed the case here).

Since all data points correspond to $\mathrm{Pe}\geq1$, the *direct* influence on longitudinal dispersion of molecular diffusion is low: It has, however, a strong indirect influence at the lower Péclet numbers investigated ($\mathrm{Pe}\lesssim10$). The transit time of the tracer inside the junctions or individual flow channels is then large enough so that molecular diffusion across the flow lines is significant: this influences strongly the redistribution of the incoming tracer between channels leaving each junction.[12] In the next section, we show that, in addition to the determination of macroscopic parameters like U, D (or l_d), the concentration maps allow one to investigate mixing processes at the pore scale or even below.

D. Tracer exchange dynamics between transverse and longitudinal channels.

The variations with the distance X from the inlet of both the mean transit time $\bar{t}(X)$ (Fig. 5) and the dispersion coefficient $D(X)$ (Fig. 6) display periodic oscillations about, respectively, an increasing linear trend and a constant value. As shown by Fig. 5(b), these oscillations are also observed at the lowest Péclet number used in our experiments, for which the rheology of the 500 ppm solution is almost Newtonian: they do not result, therefore, solely from the shear thinning properties of the fluid, although they are influenced by them. In the following, the oscillation of D is characterized by the

difference between $D(X)$ and its mean; the variation of $\bar{t}(X)$ is characterized by its difference with the linear regression line over all data points giving the mean front velocity U. At a given distance X the time corresponding to this regression is equal to X/U as shown in the insets of Figs. 5(a) and 5(b). The difference $\bar{t}(X)-X/U$ is negative when the line $X=cst$ over which $C(X,t)$ is computed contains only longitudinal channels parallel to the axis x; it is positive when the line contains both transverse channels parallel to y and junctions. The coefficient $D(X)$ is also higher than the mean value when the line $X=cst$ contains only longitudinal channels and lower when it contains both junctions and transverse channels (see the inset of Fig. 6). The oscillations of $\bar{t}(X)$ reflect the different influence of longitudinal and transverse channels on transport. As already discussed in Sec. II, in a weakly disordered square network like the present one, most convective flux takes place inside the longitudinal channels (parallel to the mean flow). The mean velocity there is significantly higher than in the transverse channels and they get saturated faster with the displacing fluid. There is therefore a time lag between the saturation of the transverse and longitudinal channels at a same distance X from the inlet, which explains the oscillations of $\bar{t}(X)$ in Fig. 5.

Moreover, the respective amplitudes of the successive minima and maxima of $\bar{t}(X)-X/U$ are found to be almost constant from one to the other. In the following, the time lags will therefore be characterized by the respecting averages δt_l and δt_{jt} over all minimal and maximal values of $\bar{t}(X)-X/U$ as displayed in the insets of Figs. 5(a) and 5(b).

In the limit of a perfect mixing at the junctions (Pe <10), fluid particles do not retain the memory of their past trajectory (i.e., whether they got previously trapped inside slow transverse channels). Therefore, the time lag for lines $X=cst$ containing transverse channels should reflect directly the residence time in an individual (slow) transverse channel, weighted by the corresponding volume fraction. As long as $\mathrm{Pe}\gg 1$ and molecular diffusion is negligible, the residence time in a given channel will be inversely proportional to the local velocity; the latter is, in turn, proportional to the mean velocity U when the Reynolds number is low enough and the linear Stokes equation is applicable. As a result, the local velocity is proportional to the mean velocity U and the time lag $\delta t_{jt}>0$ should vary as $1/U$ (similarly $\delta t_l<0$ should also vary as $1/U$). Figure 8 displays the variations of δt_{jt} and δt_l with $1/U$ for the two polymer solutions investigated: in both cases, the variation is linear for $1/U\geq 40$ s mm^{-1} (corresponding to $\mathrm{Pe}\leq 6$).

For $1/U<40$ ($\mathrm{Pe}>6$), δt_{jt} (δt_l) is higher (lower) than the values extrapolated from the linear trend for $1/U\geq 40$: the transition is observed at the same mean velocity for the two solutions. This increase of the absolute values of the time lags reflects very likely the breakdown of the assumption of perfect mixing at junctions or inside individual channels: at high Péclet numbers, a solute particle may indeed flow through several junctions and channels without moving across flow lines through transverse molecular diffusion. If the lattice is weakly disordered, the solute will remain for a longer time inside a sequence of longitudinal high-velocity channels than when there is perfect mixing at the junctions: the value of δt_l is then lower. Similarly solute particles remain trapped for a longer time in slow zones and δt_{jt} is higher than when there is good mixing at the junctions.

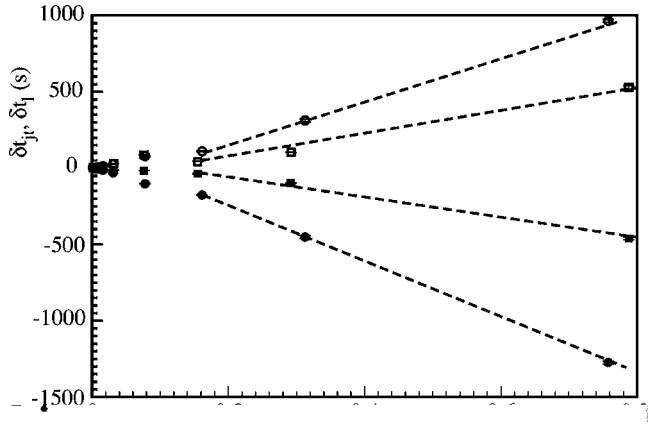

FIG. 8. Variation of δt_l (filled symbols) and δt_{jt} (open symbols) with $1/\mathrm{Pe}$. (□, ■): experiments realized with 500 ppm polymer solutions; (○, ●): 1000 ppm. Dashed lines are guides for the eyes.

Although the transition between the above two regimes takes place at the same Péclet number for both solutions, the absolute amplitude of the variations of δt_{jt} and δt_l with $1/U$ is significantly larger for the 1000 ppm one. This is a direct consequence of the different rheological properties of the two fluids, namely of the stronger shear-thinning character of the 1000 ppm solution, particularly at low flow rates. The effective viscosity of shear-thinning solutions increases much more with the polymer concentration in slow transverse channels (where the shear rate is low) than in fast longitudinal ones: as a result, the contrast between the velocities (and therefore the residence times) in the longitudinal and transverse channels is enhanced, leading to the observed increase of $|\delta t_{jt}|$ and $|\delta t_l|$. These velocity contrasts will be estimated below in Sec. V.

At the opposite limit of low velocities such that $\mathrm{Pe}<1$ ($1/U\geq 250$ s$\times$mm^{-1}), longitudinal diffusive transfer becomes significant. The increase of the residence times with $1/U$ is then limited by molecular diffusion to a value of the order of a few l^2/D_m ($\sim$1000 s): the variations of δt_{jt} and δt_l should then level off at high $1/U$ values. The lowest values of Pe are, however, still too high in our experiments to observe this effect.

These results suggest that such local observations as reported here provide important information on mixing processes at the pore scale. As pointed out recently,[7,8] these processes influence strongly, in turn, mass transfer at the macroscopic scale. In a similar perspective, the dependence of the geometry of the isoconcentration fronts on the flow velocity and on the polymer concentration will now be investigated. Their relation to local mixing in the pores will also be discussed.

E. Geometry of tracer displacement fronts

In the present experiments, the pixel size in the concentration maps is 0.4 times the mean channel width. This al-

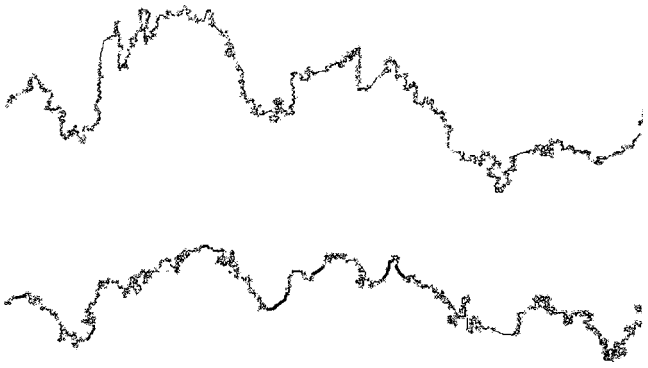

FIG. 9. Isoconcentration fronts at a mean velocity $U=0.005$ mm/s (Pe $=1.3$) for polymer solutions of concentrations 1000 ppm (upper curve) and 500 ppm (lower curve). Mean distance of tracer from inlet: $0.5\times L$ (L=model length). Flow is upward on the figure. Front widths: σ $=4.5$ mm (1000 ppm) and $\sigma=2.6$ mm (500 ppm).

lows for a study of the tracer distribution in the mixing zone at length scales varying from the size of the network down to a fraction of the pore size. For practical reasons, we shall not use the full spatial concentration distribution in the following analysis: we chose instead to characterize its spatial heterogeneity by the isoconcentration lines $c=0.5$ which may be assumed to reflect the *displacement front* geometry. Examples of such fronts determined by a thresholding procedure are displayed in Figs. 9 and 10 for Péclet numbers Pe equal to 1.3 and 32, respectively.

The width of the front parallel to the mean flow is larger for the more concentrated solution and increases with Pe. Also, at high Pe values, large spikes are visible while the front is relatively smooth at lower ones. In spite of these differences, the main geometrical features of the front are similar: large peaks and troughs are generally located at the same points for different flow velocities and polymer concentrations. This confirms that irregularities of the front

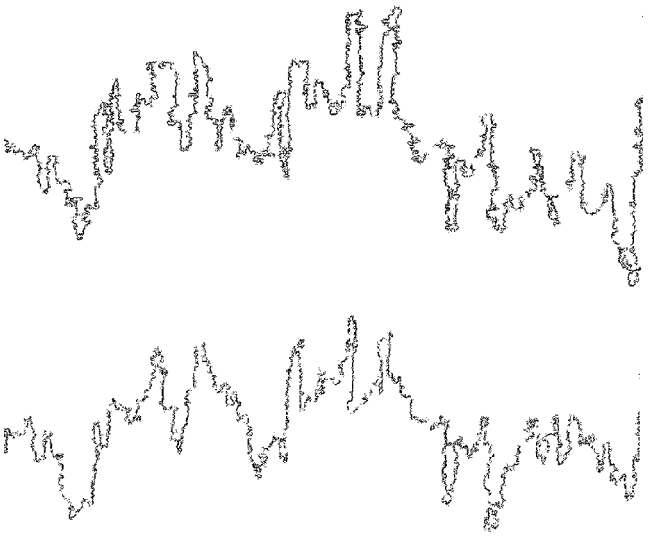

FIG. 10. Isoconcentration fronts for a mean velocity $U=0.125$ mm/s (Pe $=32$) for polymer solutions of concentrations 1000 ppm (upper curve) and 500 ppm (lower curve). Mean distance of tracer from inlet: $0.5\times L$ (L=model length). Flow is upward on the figure. Front widths: σ $=6.1$ mm (1000 ppm) and $\sigma=4.6$ mm (500 ppm).

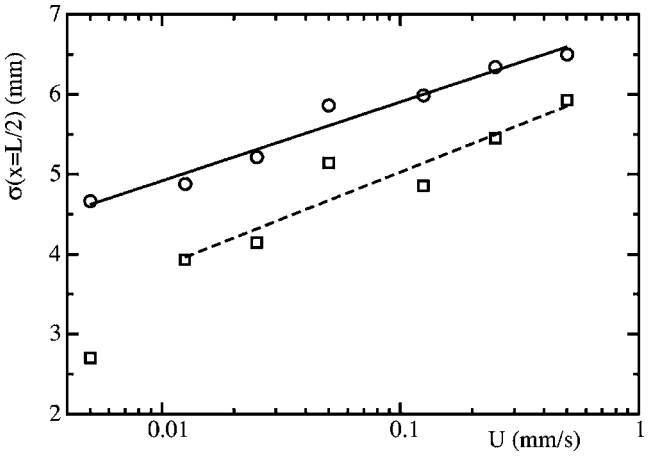

FIG. 11. Effective front width σ as a function of the mean front velocity U (mm/s) for a mean distance $\bar{x}=0.5\times L$ and polymer concentrations equal to 1000 ppm (○) and 500 ppm (□). Solid (dotted) lines: fit of the experimental data for a 1000 ppm (500 ppm) polymer solution by the equation $\sigma=a$ $+b\log(U)$ with $a=6.9\pm0.1$ and $b=0.4\pm0.05$ ($a=6.2\pm0.2$ and $b=0.5\pm0.1$).

structure are related to deterministic features of the velocity field and not to uncontrolled imperfections of the injection.

Quantitatively, the effective width of the front parallel to the flow is characterized in the following by the standard deviation $\sigma(\bar{x})$ of the distance x of its points from the inlet: $\sigma(\bar{x})$ satisfies $\sigma(\bar{x})=\langle[\bar{x}-x(y)]^2\rangle^{1/2}$ in which $\bar{x}$ is the mean value of x. In Figs. 9 and 10, $\bar{x}$ is equal to half the length of the model, and the values of σ corresponding to the curves displayed are listed in the captions. Figure 11 displays the variation of σ as a function of the mean flow velocity U for $\bar{x}=L/2$. For both solutions, the width σ increases logarithmically with U: the value of σ is larger for the 1000 ppm solution while the slope of its variation with U in Fig. 11 is slightly lower.

The values of σ are different for the two solutions because the effective viscosity decreases faster with the velocity gradients for the 1000 ppm solution than for the 500 ppm one. The ratio between the effective viscosities, and therefore the velocities in the longitudinal and transverse channels, is therefore higher, and the front width, which is directly related to this ratio, increases.

The second major feature of the front geometries at high velocity is the large amplitude of the peaks and troughs, which are smaller and narrower at lower velocities. This, too, may be explained by the reduced tracer mixing at junctions at high Péclet numbers (Sec. IV D): solute remaining for a long distance inside longitudinal, high velocity, channels contributes to the spikes while that moving through a sequence of slow lateral channels contributes to the troughs. At lower Péclet numbers, mixing is more efficient and solute particuls sample more effectively the velocity distribution: this reduces the dispersion of the transit times and, therefore, the amplitude of the peaks and troughs.

V. DISCUSSION AND CONCLUSIONS

The local analysis of the transit times and of the front geometry provide, therefore, important information on mixing inside junctions and flow channels and on its dependence

on the Péclet number. This information greatly helps one to interpret the macroscopic dispersivity measurements of Sec. IV B. Some of the features observed are specific to 2D systems while others can occur in usual 3D media.

At low Péclet numbers (typically $\mathrm{Pe} \leq 10$), the dispersivity l_d remains constant with Pe and is lower for the 500 ppm polymer solution than for the 1000 ppm one. In Secs. IV D and IV E, we have seen that, in this regime, transverse mixing in junctions and channels is very effective so that the correlation length of the motion of solute particles is of the order of the length l of individual channels. As a result, this motion may be described as a sequence of random steps of varying durations and directions inside the medium; this is the geometrical dispersion regime discussed in Sec. II and for which $D \propto \mathrm{Pe}$ ($l_d = cst$).

In this regime, the factor of 2 difference of the dispersivities for 500 and 1000 ppm solutions is likely due to enhanced velocity contrasts between the fast and slow flow regions. It is known, for instance,[17] that the mean flow velocity inside a cylindrical channel under a given pressure gradient varies as the square of the radius a for a Newtonian fluid and as $a^{1+1/n}$ for a shear thinning fluid verifying Eq. (2). Let us assume that the pressure gradient between the ends of flow channels in parallel is constant. If $\sigma(a) \ll \bar{a}$, the standard deviation δU of the mean velocities in the different channels should scale like

$$\frac{\delta U}{U} \sim \frac{1+n}{n} \frac{\sigma(a)}{\bar{a}}, \tag{4}$$

where $\sigma(a)/\bar{a}$ is the normalized standard deviation of the channel aperture (see Sec. III A). Still using the same simplistic approach, the typical standard deviation δt of the transit time along a channel of length $l = 0.67$ mm should be $l \delta U / U^2$. Estimating the dispersion coefficient D from the relation $D \sim l^2 \delta t / t^2$ ($t = l/U$) provides the order of magnitude of the dispersivity,

$$l_d \sim \frac{n+1}{n} \frac{\sigma_a}{a} l. \tag{5}$$

Since n decreases with the polymer concentration, l_d should therefore increase for a fixed aperture fluctuation $\sigma(a)/a$. Using in Eq. (5) the values of l, $\sigma(a)/a$, and n corresponding to the present experiments (Table I) leads to $l_d \simeq 0.7$ and 1 mm, respectively, for the 500 and 1000 ppm solutions. These estimations are close to the experimental values $l_d = 1 \pm 0.25$ and 1.95 ± 0.25 mm reported in Sec. IV C for the same solutions (Fig. 7). The difference may be due to the assumption of identical pressure gradients on different parallel channels used to obtain Eqs. (4) and (5).

At higher Péclet numbers $\mathrm{Pe} > 10$, l_d is no longer constant but increases with Pe. This reflects the transition toward a second dispersion regime in which mixing is less effective. One must then take into account the stretching of dye parallel to the flow by local velocity gradients in the flow section (dye moves slower in the vicinity of the walls than in the center of the channels). This stretching effect is balanced by transverse molecular diffusion, resulting in a Taylor-like dispersion mechanism (Sec. II). This effect is made significant by the increase with Pe of the correlation length of dye transport along chains of flow channels parallel to the mean flow discussed above in Secs. IV D and IV E.

The effect of the local velocity gradients is also enhanced by the specific topology of 2D micromodels. The upper and lower walls are indeed continuous and some flow lines remain close to them over their full length: as in Taylor dispersion, slow solute particles near these walls may only move away from them through molecular diffusion. Similarly, fast moving particles halfway between the walls can only reach them through transverse molecular diffusion. The large correlation length of these velocity contrasts also results in Taylor-like dispersion effects.

Yet the influence of the disorder of the medium cannot be completely neglected (since some tracer always moves into lower velocity transverse channels): the global dispersion results, therefore, from the combined effects of geometrical and Taylor dispersion. As a result, the macroscopic dispersion coefficient D follows in this regime a power law $D \propto \mathrm{Pe}^{\beta}$ of the Péclet number with an exponent $\beta \simeq 1.33$ intermediate between the values 2 and 1 corresponding, respectively, to Taylor and geometrical dispersion.

Regarding the influence of the shear thinning properties, increasing the polymer concentration enhances velocity contrasts between different flow channels while it flattens the velocity profile in individual channels. The first effect increases geometrical dispersion and is indeed observed at low Péclet numbers. The second reduces Taylor dispersion: this explains why, at higher Pe values, the values of l_d for the two polymer solutions are similar when the influence of Taylor dispersion is large.

To conclude, the dispersion measurements reported in the present work for transparent micromodels provide significant novel information on the influence of the flow velocity and fluid rheology on miscible displacements in porous media. Quantitative high-resolution optical measurements allowed for thorough studies over a broad range of length scales: in particular, it has been possible in the same experiment both to determine macroscopic parameters such as the effective dispersivity and to analyze at the pore scale the dynamics of concentration variations.

In particular, the local analysis of the time lag between the invasions of longitudinal and transverse channels of the model has allowed us to relate the transition between two dispersion regimes for $\mathrm{Pe} \simeq 10$ to variations of mixing in channel junctions. The variations of small scale structures of the displacement front with the Péclet number and the polymer concentration also provide information on the spatial correlation of transport at the local scale.

In the future, investigation of these effects at still higher resolutions should allow for detailed direct studies of mixing and flow patterns right inside individual flow channels and their junctions.

ACKNOWLEDGMENTS

We thank C. Zarcone and the "Institut de Mécanique des Fluides de Toulouse" for realizing and providing us with the micromodel used in these experiments, and G. Chauvin and

R. Pidoux for realizing the experimental setup. This work has been realized in the framework of the ECOS Sud Program No. A03-E02 and of a CNRS-CONICET Franco-Argentinian "Programme International de Cooperation Scientifique" (PICS No. 2178). One of us (M.V.D'A.) has benefited from a scholarship of the University of Buenos Aires.

[1] J. Bear, *Dynamics of Fluids in Porous Media* (Elsevier, New York, 1972).
[2] F. A. L. Dullien, *Porous Media, Fluid Transport and Pore Structure*, 2nd ed. (Academic, New York, 1991).
[3] E. Charlaix, J. P. Hulin, C. Leroy, and C. Zarcone, "Experimental study of tracer dispersion in flow through two-dimensional networks of etched capillaries," J. Phys. D **21**, 1727 (1988).
[4] "Methods in the physics of porous media," in *Experimental Methods in the Physical Sciences*, edited by P. Z. Wong (Academic, London, 1999), Vol. 35.
[5] R. Lenormand, C. Zarcone, and A. Sarr, "Mechanism of the displacement of one fluid by another in a network of capillary ducts," J. Fluid Mech. **135**, 337 (1983).
[6] A. Birovljev, K. J. Måløy, J. Feder, and T. Jøssang, "Scaling structure of tracer dispersion fronts in porous media," Phys. Rev. E **49**, 5431 (1994).
[7] D. Grubert, "Effective dispersivities for a two-dimensional periodic fracture network by a continuous time random walk analysis of single-intersection simulations," Water Resour. Res. **37**, 41 (2001).
[8] Y. Park, J. R. de Dreuzy, K. Lee, and B. Berkowitz, "Transport and intersection mixing in random fracture networks with power law length distributions," Water Resour. Res. **37**, 2493 (2001).
[9] K. S. Sorbie, P. J. Clifford, and E. R. W. Jones, "The rheology of pseudoplastic fluids in porous media using network modeling," J. Colloid Interface Sci. **130**, 508 (1989).
[10] A. Paterson, A. D'Onofrio, C. Allain, J. P. Hulin, M. Rosen, and C. Gauthier, "Tracer dispersion in a polymer solution flowing through a double porosity porous medium," J. Phys. II **6**, 1639 (1996).
[11] M. A. Freytes, A. d'Onofrio, M. Rosen, C. Allain, and J. P. Hulin, "Gravity driven instabilities in miscible non Newtonian fluid displacements in porous media," Physica A **290**, 286 (2001).
[12] V. V. Mourzenko, F. Yousefian, B. Kolbah, J. F. Thovert, and P. M. Adler, "Solute transport at fracture intersections," Water Resour. Res. **38**, 1000 (2002).
[13] B. Berkowitz, C. Naumann, and L. Smith, "Mass transfer at fracture intersections: An evaluation of mixing models," Water Resour. Res. **30**, 1765 (1994).
[14] G. I. Taylor, "Dispersion of soluble matter in solvent flowing slowly through a tube," Proc. R. Soc. London, Ser. A **219**, 186 (1953).
[15] R. Aris, "On the dispersion of a solute in a fluid flowing through a tube," Proc. R. Soc. London, Ser. A **253**, 67 (1956).
[16] M. Vartuli, J. P. Hulin, and G. Daccord, "Taylor dispersion in a polymer solution flowing in a capillary tube," AIChE J. **41**, 1622 (1995).
[17] C. B. Shah and Y. C. Yortsos, "Aspects of flow of power-law fluids in porous media," AIChE J. **41**, 1099 (1995).
[18] A. Fadili, P. Tardy, and A. Pearson, "A 3D filtration law for power-law fluids in heterogeneous porous media." J. Non-Newtonian Fluid Mech. **106**, 121 (2002).
[19] C. Bruderer and Y. Bernabé, "Network modeling of dispersion: Transition from Taylor dispersion in homogeneous networks to mechanical dispersion in very heterogeneous ones," Water Resour. Res. **37**, 897 (2001).
[20] R. L. Detwiler, H. Rajaram, and R. J. Glass, "Solute transport in variable-aperture fractures: An investigation of the relative importance of Taylor dispersion and macrodispersion." Water Resour. Res. **36**, 1611 (2000).
[21] L. de Arcangelis, J. Koplik, D. Redner, and D. Wilkinson, "Hydrodynamic dispersion in network of porous media," Phys. Rev. Lett. **57**, 996 (1986).